PET Imaging of Tumor-Associated Macrophages with ^{89}Zr-Labeled High-Density Lipoprotein Nanoparticles

Carlos Pérez-Medina[1–3], Jun Tang[3,4], Dalya Abdel-Atti[4], Brandon Hogstad[5–7], Miriam Merad[5–7], Edward A. Fisher[8], Zahi A. Fayad[3], Jason S. Lewis[4,9], Willem J.M. Mulder[3,10], and Thomas Reiner[4,9]

[1]Centro de Investigación en Red de Enfermedades Respiratorias, CIBERES, Madrid, Spain; [2]Centro Nacional de Investigaciones Cardiovasculares, CNIC, Madrid, Spain; [3]Translational and Molecular Imaging Institute, Icahn School of Medicine at Mount Sinai, New York, New York; [4]Department of Radiology, Memorial Sloan Kettering Cancer Center, New York, New York; [5]Department of Oncological Sciences, Icahn School of Medicine at Mount Sinai, New York, New York; [6]The Tisch Cancer Institute, Icahn School of Medicine at Mount Sinai, New York, New York; [7]Immunology Institute, Icahn School of Medicine at Mount Sinai, New York, New York; [8]Leon H. Charney Division of Cardiology and Marc and Ruti Bell Program in Vascular Biology, New York University School of Medicine, New York, New York; [9]Weill Cornell Medical College, New York, New York; and [10]Department of Vascular Medicine, Academic Medical Center of the University of Amsterdam, Amsterdam, The Netherlands

Tumor-associated macrophages (TAMs) are increasingly investigated in cancer immunology and are considered a promising target for better and tailored treatment of malignant growth. Although TAMs also have high diagnostic and prognostic value, TAM imaging still remains largely unexplored. Here, we describe the development of reconstituted high-density lipoprotein (rHDL)–facilitated TAM PET imaging in a breast cancer model. **Methods:** Radiolabeled rHDL nanoparticles incorporating the long-lived positron-emitting nuclide ^{89}Zr were developed using 2 different approaches. The nanoparticles were composed of phospholipids and apolipoprotein A-I (apoA-I) in a 2.5:1 weight ratio. ^{89}Zr was complexed with deferoxamine (also known as desferrioxamine B, desferoxamine B), conjugated either to a phospholipid or to apoA-I to generate ^{89}Zr-PL-HDL and ^{89}Zr-AI-HDL, respectively. In vivo evaluation was performed in an orthotopic mouse model of breast cancer and included pharmacokinetic analysis, biodistribution studies, and PET imaging. Ex vivo histologic analysis of tumor tissues to assess regional distribution of ^{89}Zr radioactivity was also performed. Fluorescent analogs of the radiolabeled agents were used to determine cell-targeting specificity using flow cytometry. **Results:** The phospholipid- and apoA-I–labeled rHDL were produced at 79% ± 13% (n = 6) and 94% ± 6% (n = 6) radiochemical yield, respectively, with excellent radiochemical purity (>99%). Intravenous administration of both probes resulted in high tumor radioactivity accumulation (16.5 ± 2.8 and 8.6 ± 1.3 percentage injected dose per gram for apoA-I– and phospholipid-labeled rHDL, respectively) at 24 h after injection. Histologic analysis showed good colocalization of radioactivity with TAM-rich areas in tumor sections. Flow cytometry revealed high specificity of rHDL for TAMs, which had the highest uptake per cell (6.8-fold higher than tumor cells for both DiO@Zr-PL-HDL and DiO@Zr-AI-HDL) and accounted for 40.7% and 39.5% of the total cellular DiO@Zr-PL-HDL and DiO@Zr-AI-HDL in tumors, respectively. **Conclusion:** We have developed ^{89}Zr-labeled TAM imaging agents based on the natural nanoparticle rHDL. In an orthotopic mouse model of breast cancer, we have demonstrated their specificity for macrophages, a result that was corroborated by flow cytometry. Quantitative macrophage PET imaging with our ^{89}Zr-rHDL imaging agents could be valuable for noninvasive monitoring of TAM immunology and targeted treatment.

Key Words: tumor-associated macrophages; ^{89}Zr; PET; high-density lipoprotein; breast cancer

J Nucl Med 2015; 56:1272–1277
DOI: 10.2967/jnumed.115.158956

Tumor-associated macrophage (TAM) immunology has become an active research field in recent years (*1,2*). Their complex role in carcinogenesis generally leads to disease progression in most cancers (*3*), which share some similar pathologic mechanisms and, often, high TAM burden has been associated with poor prognosis (*4*). During cancer progression, circulating monocytes and macrophages are recruited to tumors, where they differentiate under the influence of a milieu of growth factors and cytokines (*5*). In this process, TAMs themselves become critical modulators of the tumor microenvironment, as they foster tumor growth (*6*), immune suppression, metastasis (*7*), and chemoresistance (*1*) by generating tumor-promoting conditions. TAMs' significant implication in modulating the immune system response to tumor growth has led to various TAM-targeting therapies (*8*), some of which are being evaluated in the clinic (*2,9,10*).

For these reasons, specific and quantifiable TAM imaging agents are critical to evaluate the efficacy of TAM-targeting therapies and to facilitate prognosis of TAM-driven cancers. In fact, imaging of macrophages as key mediators of the inflammatory response is already an active area of research. Several nanoparticulate materials have been studied as such imaging agents (*11*). Among others, several iron oxide–based MR imaging probes (*12,13*), as well as ^{64}Cu-labeled/mannose-functionalized liposomes (*14*), and nanobodies (*15*) have been applied. Still, despite these efforts, clinical imaging of TAMs remains largely unexplored.

High-density lipoprotein (HDL) is a natural nanoparticle that has been exploited for MR molecular imaging of the atherosclerotic

Received Apr. 7, 2015; revision accepted Jun. 4, 2015.
For correspondence or reprints contact either of the following:
Thomas Reiner, Department of Radiology, Memorial Sloan Kettering Cancer Center, 1275 York Ave., New York, NY 10065.
E-mail: reinert@mskcc.org
W.J.M. Mulder, Translational and Molecular Imaging Institute, Icahn School of Medicine at Mount Sinai, One Gustave L. Levy Place, Box 1234, New York, NY 10029.
E-mail: willem.mulder@mssm.edu
Published online Jun. 25, 2015.

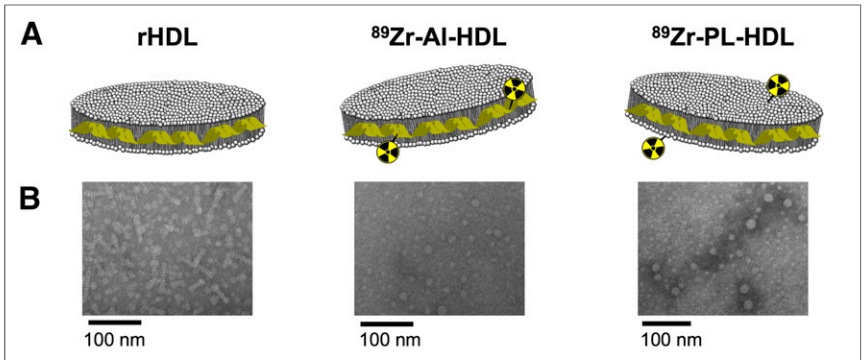

C

	ApoA-I	DMPC	DSPE-DFO	Size/d.nm	PDI	Z-Potential/mV
rHDL	1%	99%	-	8.7 ± 0.9	0.32 ± 0.05	-14.6 ± 3.2
^{89}Zr-AI-HDL	1%	99%	-	8.5 ± 1.1	0.20 ± 0.06	-16.2 ± 1.6
^{89}Zr-PL-HDL	1%	98%	1%	8.5 ± 0.8	0.31 ± 0.11	-13.5 ± 6.6

FIGURE 1. Structure and composition of rHDL and ^{89}Zr-HDL nanotracers. (A) Schematic of rHDL (left), ^{89}Zr-AI-HDL (middle), and ^{89}Zr-PL-HDL (right). (B) Transmission electron microscopy images of rHDL (left), Zr-AI-HDL (middle), and Zr-PL-HDL (right). (C) Composition (in mol %), size, polydispersity index (PDI), and surface charge of rHDL, ^{89}Zr-AI-HDL, and ^{89}Zr-PL-HDL. Data are presented as mean ± SD ($n \geq 3$).

plaque, and its specificity for macrophages has been established (*16*). Furthermore, in 2 recent studies, we have demonstrated its ability to deliver an antiinflammatory drug to macrophages in atherosclerotic plaques with great specificity (*17,18*). To enable HDL use for quantitative PET imaging of TAMs, we here present the design and synthesis of 2 different ^{89}Zr-modified reconstituted HDL (rHDL) nanotracers and their in vivo evaluation in an orthotopic mouse model of breast cancer. Specifically, we labeled either its protein component (apolipoprotein A-I [apoA-I]) or its phospholipid load and examined the agent's TAM targeting using in vivo PET imaging and ex vivo analyses, including immunohistochemistry. Additionally, we prepared 2 fluorescent analogs of our radiolabeled ^{89}Zr-rHDL nanotracers to allow us to gain insight into their cellular targets by flow cytometry.

MATERIALS AND METHODS

A detailed description of the preparation of reconstituted HDL nanoparticles; their radiolabeling; and in vitro, in vivo, and ex vivo experiments can be found in the supplemental data (available at http://jnm.snmjournals.org). All animal experiments were done in accordance with protocols approved by the Institutional Animal Care and Use Committee of Memorial Sloan Kettering Cancer Center and followed National Institutes of Health guidelines for animal welfare.

RESULTS

Preparation of rHDL Nanoparticles and Radiolabeling with ^{89}Zr

rHDL (Fig. 1A) nanoparticles were prepared by mixing DMPC (dimyristoylphosphatidylcholine) vesicles with apoA-I, resulting in discoidal particles with a mean hydrodynamic diameter of 8.7 ± 0.9 nm ($n = 6$), as measured by dynamic light scattering. The labeling of rHDL nanoparticles with ^{89}Zr required prior modification of its components with the chelator deferoxamine (DFO; also known as desferrioxamine B, desferoxamine B). Conjugation of DFO to apoA-I was achieved via reaction of its lysine amino groups with DFO-*p*-NCS on preformed rHDL particles. The resulting DFO-apoA-I@rHDL had a diameter of 8.9 ± 1.1 nm ($n = 5$). To label the phospholipid cargo, we incorporated the phospholipid chelator 1,2-distearoyl-sn-glycero-3-phosphoethanolamine (DSPE)-DFO in the formulation at the expense of DMPC. Thus, we obtained 1% DSPE-DFO@rHDL with a mean diameter of 8.6 ± 1.3 nm ($n = 5$). The retention time of the 2 modified nanoparticles on size-exclusion chromatography was identical and the same as unmodified rHDL, which corresponds to a species of estimated molecular weight of 150 kDa. Transmission electron microscopy images showed that both modified rHDL nanoparticles retained the discoidal shape (Fig. 1B). Radiolabeling of both DFO-apoA-I@rHDL and 1% DSPE-DFO@rHDL proceeded in high yield. apoA-I–labeled rHDL (^{89}Zr-AI-HDL, Fig. 1A) was obtained in 94% ± 6% ($n = 6$) radiochemical yield; for phospholipid-labeled rHDL (^{89}Zr-PL-HDL, Fig. 1A), radiochemical yield was 79% ± 13% ($n = 6$). The composition, size, and ζ-potential of rHDL and the radiolabeled nanoparticles described in this study are shown in Figure 1C. Radiochemical purity was greater than 99% in both cases (Figs. 2A and 2B). As expected, the incubation of plain, unmodified rHDL particles with ^{89}Zr-oxalate in the same conditions resulted in no detectable radiolabeling.

In Vitro Serum Stability of ^{89}Zr-Labeled HDL Nanotracers

To study label dynamics in vitro, the radiolabeled nanoparticles were incubated at 37°C in fetal bovine serum. Analysis by size-exclusion chromatography proved the dynamic nature of these nanoparticles. For ^{89}Zr-AI-HDL, a new peak eluting at the same retention time as free apoA-I was detected. The ratio between ^{89}Zr-AI-HDL and this species remained largely constant over time. Another species of molecular weight greater than 300 kDa was observed at all time points. ^{89}Zr-PL-HDL showed a similar dynamic behavior, and a peak corresponding to larger particles of molecular weight greater than 300 kDa was also observed at all time points. Interestingly, activity directly associated with albumin was not detectable until 8 h, and in any case most of it (63.3% ± 1.5%)

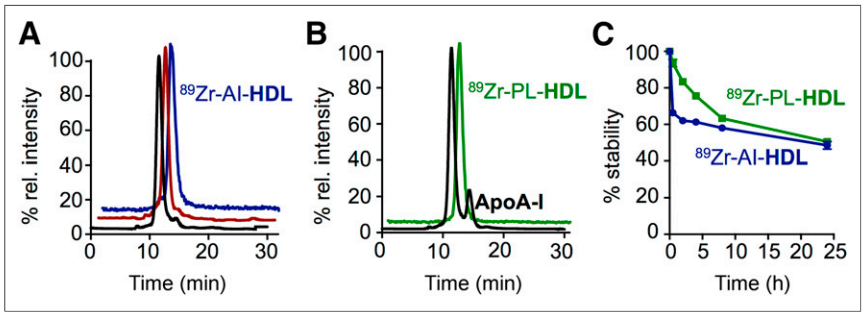

FIGURE 2. Radiosynthesis and in vitro stability of ^{89}Zr-HDL nanotracers. Size-exclusion chromatograms showing coelution of plain rHDL (black trace), DFO-apoA-I@rHDL (red trace), and ^{89}Zr-AI-HDL (blue, radioactive trace) (A) and coelution of 1% DSPE-DFO@rHDL (black trace) and ^{89}Zr-PL-HDL (green, radioactive trace) (B). (C) In vitro serum stability of ^{89}Zr-HDL nanotracers at 37°C.

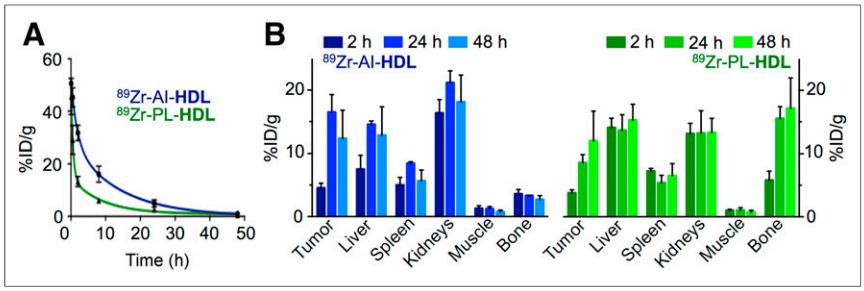

FIGURE 3. Pharmacokinetics and biodistribution of ^{89}Zr-HDL nanotracers. (A) Blood time–activity curve for ^{89}Zr-AI-HDL and ^{89}Zr-PL-HDL (n = 3). (B) Radioactivity distribution in selected tissues of ^{89}Zr-AI-HDL (blue) and ^{89}Zr-PL-HDL (green) in mice bearing orthotopic breast cancer tumors, expressed as %ID/g ± SD ($n \geq 3$).

remained bound to HDL particles (Fig. 1C). The release of small radiolabeled species was detectable after 24 h for ^{89}Zr-AI-HDL (5.5% ± 0.7%, n = 3) and after 2 h for ^{89}Zr-PL-HDL (3.3% ± 0.6%, n = 3, then reached 11.7% ± 6.4%, n = 3, after 24 h). The detection of the small radiolabeled species could be due to release of ^{89}Zr from its DFO complex or a result of the degradation of the thiourea bond in the presence of oxidizing chlorinated species (*19*) resulting in the detachment of the ^{89}Zr-DFO unit. Collectively, however, these data suggest that both ^{89}Zr-AI-HDL and ^{89}Zr-PL-HDL are sufficiently stable to allow adequate in vivo evaluation.

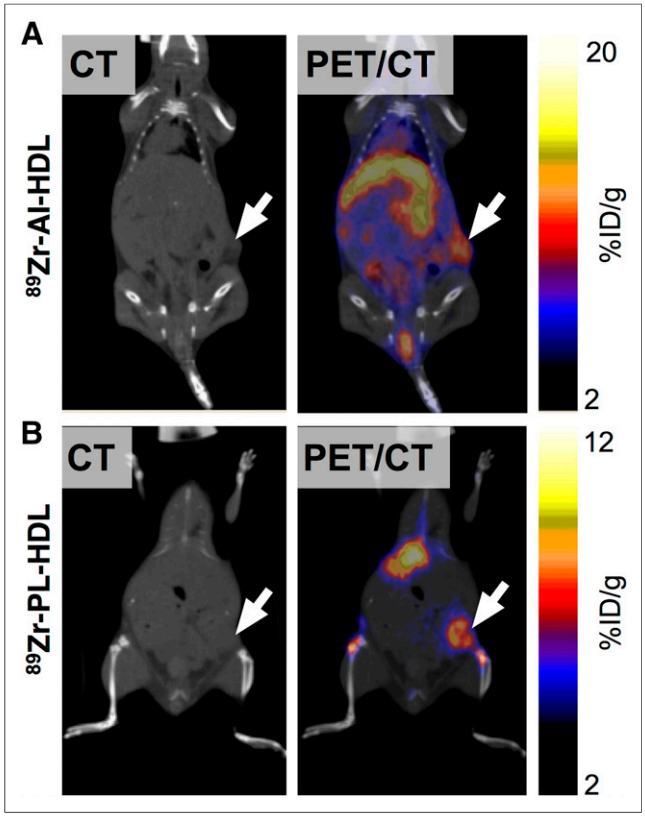

FIGURE 4. Accumulation of ^{89}Zr-HDL nanotracers in tumor tissues can be visualized by in vivo PET imaging. CT (left) and PET/CT fusion (right) images of ^{89}Zr-AI-HDL (A) and ^{89}Zr-PL-HDL (B) obtained at 24 h after injection in mice bearing orthotopic 4T1 tumors (indicated by arrows).

Pharmacokinetics and Biodistribution of ^{89}Zr-Labeled HDL Nanotracers

Blood radioactivity clearance was markedly different, depending on whether the radiolabel was attached to apoA-I or the phospholipid of rHDL, indicating that the nanoparticle might be not only passively delivered but also actively distributed, governed by its natural biologic function. The weighted half-life value measured for ^{89}Zr-AI-HDL was 5.7 h, nearly 3 times longer than that shown by ^{89}Zr-PL-HDL, with a half-life of 2.0 h (Fig. 3A). Tissue radioactivity distribution in female B6 mice bearing orthotropic 4T1-induced breast tumors was determined at 2, 24, and 48 h after administration. A selection of tissues is shown in Figure 3B for both formulations, and a complete list of values can be found in the supplemental data (Supplemental Tables 1 and 2). As expected from their blood half-lives, most of the radioactivity remains in blood at 2 h after injection. Significant accumulation was also observed in the kidneys (16.4 ± 2.1 percentage injected dose per gram [%ID/g] [^{89}Zr-AI-HDL] and 13.1 ± 1.6 %ID/g [^{89}Zr-PL-HDL]), liver (significantly higher for ^{89}Zr-PL-HDL [14.1 ± 1.5 %ID/g] than ^{89}Zr-AI-HDL [7.51 ± 2.21 %ID/g]), and, to a lesser extent, spleen (5.0 ± 1.2 and 7.2 ± 0.4 %ID/g, respectively). Tumor uptake at this time point was below 5% for both tracers. At 24 h after injection, blood activity levels had dropped to 5.30 ± 0.94 and 2.19 ± 0.23 %ID/g for ^{89}Zr-AI-HDL and ^{89}Zr-PL-HDL, respectively. A dramatic increase in tumor uptake can be observed for ^{89}Zr-AI-HDL, reaching 16.5 ± 2.8 %ID/g, whereas that of ^{89}Zr-PL-HDL was 8.6 ± 1.3 %ID/g. Kidney uptake was high for both nanotracers, but it was significantly higher for ^{89}Zr-AI-HDL at 21.2 ± 1.9 %ID/g. Whole-bone activity for ^{89}Zr-PL-HDL went up to 15.5 ± 1.9 %ID/g at this time point. Liver and spleen still retained a significant amount of activity. At 48 h after injection, liver, spleen, and kidney uptake was statistically identical for both radiolabeling approaches. Similarly, tumor uptake was 12.3 ± 4.5 %ID/g for ^{89}Zr-AI-HDL and 12.0 ± 4.7 %ID/g for ^{89}Zr-PL-HDL. The biggest discrepancy in biodistribution profiles at 48 h remained bone uptake, which was 17.1 ± 4.8 %ID/g for ^{89}Zr-PL-HDL and remained at 2.70 ± 0.62 %ID/g for ^{89}Zr-AI-HDL. We determined that 3.6% ± 1.1% of this uptake originated from bone marrow, leaving 96.4% ± 1.1% associated with mineral bone, whereas for ^{89}Zr-AI-HDL the fraction originating from bone marrow was 27.8% ± 4.1%.

In Vivo Imaging of ^{89}Zr-Labeled HDL Nanotracers

PET imaging corroborated the observations obtained in ex vivo experiments (Fig. 4). The images collected at 24 h after injection show strong liver, kidney, and tumor uptake for both nanotracers. Quantitative PET data (Supplemental Fig. 1) were essentially in agreement with the biodistribution results. When PET was used, tumor uptake values were significantly higher for ^{89}Zr-AI-HDL at 16.7 ± 1.6 %ID/g (n = 4) than for ^{89}Zr-PL-HDL (9.9 ± 0.5 %ID/g, n = 4). PET-quantified liver and kidney uptake was higher for ^{89}Zr-AI-HDL (20.8 ± 2.9 and 29.3 ± 11.5 %ID/g [n = 4], respectively) than for ^{89}Zr-PL-HDL (19.7 ± 2.5 and 13.0 ± 2.3 %ID/g [n = 4]). PET-quantified blood activity concentrations, measured in the cardiac chambers, were significantly higher than those obtained from ex vivo experiments. At this time point, radioactivity in blood was

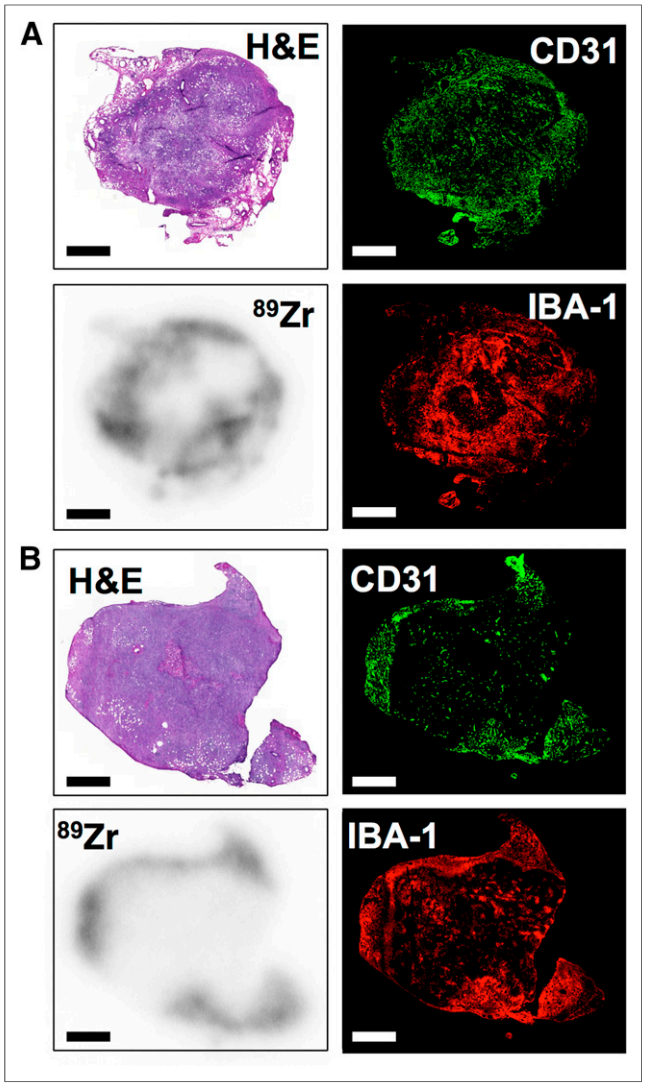

FIGURE 5. ^{89}Zr-HDL nanotracers accumulate in TAM-rich areas. Ex vivo histologic analysis of tumor sections at 24 h after administration of HDL nanotracers, showing hematoxylin and eosin (H&E) staining (top left), immunofluorescence for CD31 (top right) and IBA-1 (bottom right), and autoradiography (bottom left) for ^{89}Zr-AI-HDL (A) and ^{89}Zr-PL-HDL (B). Scale bar = 2 mm.

7.9 ± 1.6 %ID/g (n = 4) for ^{89}Zr-AI-HDL and 4.7 ± 1.5 %ID/g (n = 4) for ^{89}Zr-PL-HDL, and this difference was statistically significant.

Histologic analysis of tumor sections collected at 24 h after injection allowed us to establish regional distribution of both nanotracers (Fig. 5). Areas with high ^{89}Zr deposition are highly vascularized, as shown by colocalization of CD31 and autoradiography (Figs. 5A and 5B). However, staining for Iba-1 (Figs. 5A and 5B) showed that particularly ^{89}Zr-PL-HDL had also a high degree of colocalization to macrophage-rich areas (Fig. 5B).

Cellular Distribution of ^{89}Zr-Labeled HDL Nanotracers

The intercellular distribution of the ^{89}Zr-labeled rHDL probes was determined by flow cytometry with their respective nonradioactive analogs Zr-AI-HDL and Zr-PL-HDL. Both were labeled with a fluorescent tag (DiO), using a previously reported procedure (*17,18*). The labeled nanoparticles DiO@Zr-AI-HDL and DiO@Zr-PL-HDL had the same retention time as their radiolabeled counterparts ^{89}Zr-AI-HDL and ^{89}Zr-PL-HDL and as the unlabeled, plain rHDL using size-exclusion chromatography. We used a robust flow cytometry gating procedure to identify HDL levels in 7 relevant cell types, including TAMs, monocyte-derived cells, monocytes, dendritic cells, T cells, endothelial cells (ECs), and tumor cells (Supplemental Fig. 2). We found the highest HDL uptake by TAMs, with HDL levels 3.5-fold (DiO@Zr-AI-HDL, $P < 0.01$) and 4.1-fold (DiO@Zr-PL-HDL, $P < 0.01$) higher than monocyte-derived cells; 19.0-fold ($P < 0.01$) and 29.1-fold ($P < 0.01$) higher than monocytes; 5.9-fold ($P < 0.001$) and 6.5-fold ($P < 0.001$) higher than dendritic cells ($P < 0.05$); 124.2-fold ($P < 0.01$) and 164.8-fold ($P < 0.01$) higher than T cells; 6.3-fold ($P < 0.01$) and 4.9-fold ($P < 0.001$) higher than ECs; and 6.8-fold ($P < 0.01$) and 6.8-fold ($P < 0.001$) higher than tumor cells (Fig. 6). In this tumor model, TAMs accounted for 7.0% ± 4.4% of total live cells but made up 40.7% ± 12.9% (DiO@Zr-PL-HDL) and 39.5% ± 4.1% (DiO@Zr-AI-HDL) of total intracellular HDL in all live cells. Using fluorescent, unmodified rHDL (DiO@rHDL), we found a strikingly similar cell targeting pattern to the 2 Zr-labeled fluorescent HDL formulations (Supplemental Fig. 3), suggesting that Zr modification totally preserves the intrinsic TAM-targeting ability of rHDL. These data compellingly show that HDL not only efficiently accumulated in tumors but also specifically targeted TAMs.

DISCUSSION

The aim of this study was to design a radiolabeled HDL-based nanoparticle to selectively target TAMs, capitalizing on HDL's biologic function (*20*) rather than passive accumulation (via the enhanced permeability and retention effect) (*11*) or hijacking a biomarker for targeted imaging (*15*). For this, we explored 2 different HDL-labeling approaches: attachment of the radiolabel to apoA-I, the main apolipoprotein component of HDL, and radiolabeling of the phospholipid load of the particle. We chose ^{89}Zr as the radioisotope because its physical half-life (78.4 h) matches the long biologic half-life of HDL.

Both radiolabeling approaches required different DFO-modified building blocks. The first one was synthesized by conjugation of DFO to apoA-I via reaction of the rHDL particles with DFO-*p*-NCS. The second one, the phospholipid-based chelator DSPE-DFO, was prepared as recently described by us (*21*). These modifications had no measurable effect on the size, compared with plain rHDL (Fig. 1C). In both cases, the radiolabeling of the modified precursors resulted in the permanent association of the radioisotope to a particle fraction of an estimated molecular weight of 150 kDa. This molecular weight is in concordance with the expected molecular weight of discoidal HDL (*22*).

Biologic evaluation was performed in mice and provided insight into the nanoparticles' pharmacokinetics. The blood residence time differences likely reflect the different behavior of both components in natural HDL. The protein-labeled ^{89}Zr-AI-HDL showed a significantly longer blood half-life (5.7 h) as opposed to the 2.0 h half-life observed for ^{89}Zr-PL-HDL. It is well known that phospholipids transported by HDL exchange with other lipoproteins (*23*) before they are ultimately cleared from circulation when delivered to their targets. On the other hand, the net internalization and catabolic rate of apoA-I are low, thus lengthening its circulation time, compared with the phospholipid-labeled nanoparticle (*24*). As a result, the ^{89}Zr-AI-HDL–associated radioactivity half-life seems to match the slow turnover of HDL in the organism.

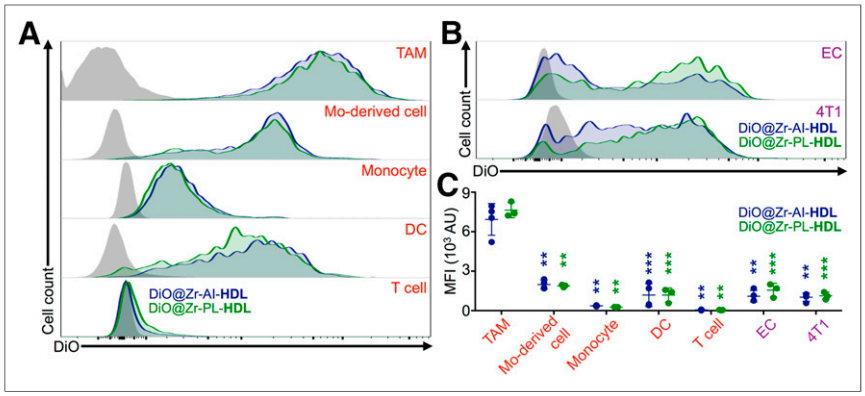

FIGURE 6. Both DiO@Zr-PL-HDL and DiO@Zr-AI-HDL preferentially target tumor-associated macrophages. 4T1 cell–induced orthotopic breast tumors were used to isolate single cells. (A) Representative DiO levels in 5 immune cells, namely TAMs, monocyte-derived cells (Mo-derived cells), monocytes, dendritic cells (DCs), and T cells. (B) Representative DiO levels in ECs and tumor cells (4T1). Cells from a phosphate-buffered saline–injected mouse served as controls (gray histograms to left). (C) Quantification of DiO levels presented as mean fluorescence intensity (MFI). Importantly, no statistical significance was found when comparing DiO levels of same cell type from 2 HDL formulations. Statistics were calculated with 2-tailed Student *t* test with unequal variance by comparing with TAM from same group. $^{**}P < 0.01$. $^{***}P < 0.001$.

The breast cancer cell line 4T1 was chosen as a relevant breast cancer model to evaluate TAM targeting, because high TAM concentrations in tumors are associated with poor prognosis in this type of cancer (*2*). Acute radioactivity distribution in tissues in tumor-bearing mice provided blood-clearance profiles similar to the ones observed in blood half-life experiments. By 48 h after injection, less than 1 %ID/g remained in circulation (0.98 ± 0.25 vs. 0.49 ± 0.06 %ID/g for ^{89}Zr-AI-HDL and ^{89}Zr-PL-HDL, respectively). The high accumulation of radioactivity observed in the kidney, especially for ^{89}Zr-AI-HDL, is in agreement with previous animal studies (*25,26*). Kidneys play an important role in apoA-I catabolism, probably via the proximal renal tubules, where apoA-I is taken up and degraded (*27*). apoA-I is thus filtered through the glomerular basement membranes, followed by proximal tubule uptake, enabling endocytosis of HDL proteins (*28*). In fact, a higher glomerular filtration rate is associated with low HDL and apoA-I levels in humans (*29*).

Tumor uptake was high for both formulations, peaking at 16.5 ± 2.8 %ID/g at 24 h after injection for ^{89}Zr-AI-HDL and 12.0 ± 4.7 %ID/g at 48 h after injection for ^{89}Zr-PL-HDL. High accumulation of radioactivity in the bones of mice injected with ^{89}Zr-PL-HDL was observed. For ^{89}Zr-AI-HDL, whole-bone uptake remained below 4 %ID/g at all time points, but a progressive increase was observed for ^{89}Zr-PL-HDL, reaching 17 %ID/g at 48 h after injection. This radioactivity accumulation in the bone was mainly associated with mineral bone for both probes, as less than 5% and 30% of whole-bone activity was taken up by bone marrow for ^{89}Zr-PL-HDL and ^{89}Zr-AI-HDL, respectively. The high accumulation of activity in the mineral component of the bone has been reported for other long-circulating ^{89}Zr-labeled agents (*30,31*) and seems to be the result of liberation of ^{89}Zr from its chelator (*32*). These data were largely in agreement with the respective PET imaging signatures. Intense signals were observed in the kidneys and liver, as well as tumor, at 24 h after injection (Fig. 4). Statistically significant differences were found for blood and tumor PET-derived uptake values between the 2 nanotracers. For ^{89}Zr-PL-HDL, radioisotope uptake was also observed in the skeleton and joints mirroring ex vivo results. Most notably, ex vivo analysis of tumor sections allowed us to evaluate the nanoparticles' spatial and cell type distributions. Thus, both ^{89}Zr-PL-HDL and ^{89}Zr-AI-HDL seemed to accumulate in macrophage-rich regions, as evidenced by the colocalization of radioactivity to Iba-1–positive areas (Fig. 5).

Because histologic analysis data are inherently qualitative in nature, we decided to further quantitatively elucidate cellular specificity by flow cytometry using fluorescently labeled analogs of the radiolabeled nanotracers modified with nonradioactive zirconium. Flow cytometry analysis of a comprehensive panel of biomarkers allowed us to differentiate the particles' preference for 7 different cell types: TAMs, ECs, 4T1 tumor cells, monocyte-derived cells, monocytes, dendritic cells, and T cells (Fig. 6). The variations in fluorescence intensities among the different cell types likely reflect how HDL nanoparticles interact with their targets. Similar to histologic analysis, HDL preferentially targeted immune cells, particularly macrophages, followed by monocyte-derived cells and dendritic cells. Monocytes, T cells, ECs, and tumor cells were only marginally targeted (Fig. 6C). Moreover, the targeting pattern of both Zr-labeled fluorescent analogs was similar to that of the unmodified version (Supplemental Fig. 3). These results, in conjunction with those observed on histologic analysis, compellingly indicate that Zr-modified rHDL nanoparticles retain their biologic function and that they target macrophages with high specificity.

CONCLUSION

We have developed 2 high-yielding radiolabeling strategies to generate ^{89}Zr-HDL nanoparticles and compared them in extensive studies. PET imaging allowed noninvasive visualization of the nanotracers' high accumulation in tumors, and ex vivo histologic and flow cytometry analyses confirmed TAMs as their main target. The development of quantifiable macrophage imaging agents can meet important scientific and clinical needs, including more accurate diagnoses, prognoses, and improved treatment monitoring. We therefore believe that our imaging agents could ultimately be of high value for noninvasive in vivo evaluation of TAM burden, not only in preclinical but also in clinical settings.

DISCLOSURE

The costs of publication of this article were defrayed in part by the payment of page charges. Therefore, and solely to indicate this fact, this article is hereby marked "advertisement" in accordance with 18 USC section 1734. Financial support was provided by the NIH (K25 EB016673, R01 HL118440, R01 HL125703, R01 CA155432, P30 CA008748), the Brain Tumor Center of the Memorial Sloan Kettering Cancer Center, the Nanotechnology Center for Molecular Imaging and Nanotechnology, the CNIC CardioImage program, and NWO Vidi 91713324. No other potential conflict of interest relevant to this article was reported.

ACKNOWLEDGMENTS

We thank the Small Animal Imaging Core, the Radiochemistry and Molecular Imaging Probes Core, and the Molecular Cytology Core at Memorial Sloan Kettering Cancer Center as well as the flow cytometry facility of The Tisch Cancer Institute of Icahn School of Medicine at Mount Sinai for support. We also thank the NIH, the Brain Tumor Center of Memorial Sloan-Kettering Cancer as well as the Nanotechnology Center for Molecular Imaging and Nanotechnology for their generous funding, and the CNIC CardioImage program. In addition, thanks to Christopher Irwin for his help with biodistribution experiments.

REFERENCES

1. De Palma M, Lewis CE. Macrophage regulation of tumor responses to anticancer therapies. *Cancer Cell.* 2013;23:277–286.
2. Tang X. Tumor-associated macrophages as potential diagnostic and prognostic biomarkers in breast cancer. *Cancer Lett.* 2013;332:3–10.
3. Mantovani A, Locati M. Tumor-associated macrophages as a paradigm of macrophage plasticity, diversity, and polarization: lessons and open questions. *Arterioscler Thromb Vasc Biol.* 2013;33:1478–1483.
4. Chen Q, Zhang XH, Massague J. Macrophage binding to receptor VCAM-1 transmits survival signals in breast cancer cells that invade the lungs. *Cancer Cell.* 2011;20:538–549.
5. Franklin RA, Liao W, Sarkar A, et al. The cellular and molecular origin of tumor-associated macrophages. *Science.* 2014;344:921–925.
6. Coffelt SB, Hughes R, Lewis CE. Tumor-associated macrophages: effectors of angiogenesis and tumor progression. *Biochim Biophys Acta.* 2009;1796:11–18.
7. Condeelis J, Pollard JW. Macrophages: obligate partners for tumor cell migration, invasion, and metastasis. *Cell.* 2006;124:263–266.
8. Ries CH, Cannarile MA, Hoves S, et al. Targeting tumor-associated macrophages with anti-CSF-1R antibody reveals a strategy for cancer therapy. *Cancer Cell.* 2014;25:846–859.
9. Noy R, Pollard JW. Tumor-associated macrophages: from mechanisms to therapy. *Immunity.* 2014;41:49–61.
10. Zhang QW, Liu L, Gong CY, et al. Prognostic significance of tumor-associated macrophages in solid tumor: a meta-analysis of the literature. *PLoS ONE.* 2012;7:e50946.
11. Weissleder R, Nahrendorf M, Pittet MJ. Imaging macrophages with nanoparticles. *Nat Mater.* 2014;13:125–138.
12. Daldrup-Link H, Coussens LM. MR imaging of tumor-associated macrophages. *OncoImmunology.* 2012;1:507–509.
13. Leimgruber A, Berger C, Cortez-Retamozo V, et al. Behavior of endogenous tumor-associated macrophages assessed in vivo using a functionalized nanoparticle. *Neoplasia.* 2009;11:459–468.
14. Locke LW, Mayo MW, Yoo AD, Williams MB, Berr SS. PET imaging of tumor associated macrophages using mannose coated ^{64}Cu liposomes. *Biomaterials.* 2012;33:7785–7793.
15. Movahedi K, Schoonooghe S, Laoui D, et al. Nanobody-based targeting of the macrophage mannose receptor for effective in vivo imaging of tumor-associated macrophages. *Cancer Res.* 2012;72:4165–4177.
16. Skajaa T, Cormode DP, Falk E, Mulder WJ, Fisher EA, Fayad ZA. High-density lipoprotein-based contrast agents for multimodal imaging of atherosclerosis. *Arterioscler Thromb Vasc Biol.* 2010;30:169–176.
17. Duivenvoorden R, Tang J, Cormode DP, et al. A statin-loaded reconstituted high-density lipoprotein nanoparticle inhibits atherosclerotic plaque inflammation. *Nat Commun.* 2014;5:3065.
18. Tang J, Lobatto ME, Hassing S, et al. Inhibiting macrophage proliferation suppresses atherosclerotic plaque inflammation. *Sci Adv.* 2015;1:e1400223.
19. Vosjan MJ, Perk LR, Visser GW, et al. Conjugation and radiolabeling of monoclonal antibodies with zirconium-89 for PET imaging using the bifunctional chelate p-isothiocyanatobenzyl-desferrioxamine. *Nat Protoc.* 2010;5:739–743.
20. Marcel YL, Ouimet M, Wang MD. Regulation of cholesterol efflux from macrophages. *Curr Opin Lipidol.* 2008;19:455–461.
21. Pérez-Medina C, Abdel-Atti D, Zhang Y, et al. A modular labeling strategy for in vivo PET and near-infrared fluorescence imaging of nanoparticle tumor targeting. *J Nucl Med.* 2014;55:1706–1711.
22. Chen B, Ren X, Neville T, et al. Apolipoprotein AI tertiary structures determine stability and phospholipid-binding activity of discoidal high-density lipoprotein particles of different sizes. *Protein Sci.* 2009;18:921–935.
23. Illingworth DR, Portman OW. Exchange of phospholipids between low and high density lipoproteins of squirrel monkeys. *J Lipid Res.* 1972;13:220–227.
24. Marsh JB, Welty FK, Schaefer EJ. Stable isotope turnover of apolipoproteins of high-density lipoproteins in humans. *Curr Opin Lipidol.* 2000;11:261–266.
25. Glass CK, Pittman RC, Keller GA, Steinberg D. Tissue sites of degradation of apoprotein A-I in the rat. *J Biol Chem.* 1983;258:7161–7167.
26. Braschi S, Neville TA, Maugeais C, Ramsamy TA, Seymour R, Sparks DL. Role of the kidney in regulating the metabolism of HDL in rabbits: evidence that iodination alters the catabolism of apolipoprotein A-I by the kidney. *Biochemistry.* 2000;39:5441–5449.
27. Dallinga-Thie GM, Van 't Hooft FM, Van Tol A. Tissue sites of degradation of high density lipoprotein apolipoprotein A-IV in rats. *Arteriosclerosis.* 1986;6:277–284.
28. Hammad SM, Barth JL, Knaak C, Argraves WS. Megalin acts in concert with cubilin to mediate endocytosis of high density lipoproteins. *J Biol Chem.* 2000;275:12003–12008.
29. Krikken JA, Gansevoort RT, Dullaart RP. Lower HDL-C and apolipoprotein A-I are related to higher glomerular filtration rate in subjects without kidney disease. *J Lipid Res.* 2010;51:1982–1990.
30. Zeglis BM, Mohindra P, Weissmann GI, et al. Modular strategy for the construction of radiometalated antibodies for positron emission tomography based on inverse electron demand Diels-Alder click chemistry. *Bioconjug Chem.* 2011;22:2048–2059.
31. Chang AJ, Desilva R, Jain S, Lears K, Rogers B, Lapi S. ^{89}Zr-radiolabeled trastuzumab imaging in orthotopic and metastatic breast tumors. *Pharmaceuticals (Basel).* 2012;5:79–93.
32. Abou DS, Ku T, Smith-Jones PM. In vivo biodistribution and accumulation of ^{89}Zr in mice. *Nucl Med Biol.* 2011;38:675–681.